Constraints on thermal state and composition of the Earth's lower mantle from electromagnetic impedances and seismic data

Olivier Verhoeven, Antoine Mocquet, Pierre Vacher, A. Rivoldini, Michel Menvielle, Pierre-André Emmanuel François Arrial, Gael Choblet, Pascal Tarits, V. Dehant, T. van Hoolst

Constraints on thermal state and composition of the Earth's lower mantle from electromagnetic impedances and seismic data

O. Verhoeven,[1,2] A. Mocquet,[2] P. Vacher,[2] A. Rivoldini,[1,3] M. Menvielle,[4] P.-A. Arrial,[2] G. Choblet,[2] P. Tarits,[5] V. Dehant,[1,3] and T. Van Hoolst[1]

Received 7 March 2008; revised 18 September 2008; accepted 12 January 2009; published 10 March 2009.

[1] Despite the tight constraints put by seismology on the elastic properties of the Earth's lower mantle, its mineralogical composition and thermal state remain poorly known because the interpretation of seismic measurements suffers from the trade-off between temperature, iron content, and mineralogical composition. In order to overcome this difficulty, we complement seismic data with electromagnetic induction data. The latter data are mostly sensitive to temperature and iron content, while densities and acoustic speeds mostly constrain the mineralogy. A 0.5 log unit increase in electrical conductivity can be caused either by a 400 K increase of the temperature or by an increase of iron content from 10% to 12.5%. Acoustic velocity is only marginally sensitive to temperature but it increases by 0.8 km s^{-1} on average as the perovskite fraction increases from 50% to 100%. Olsen's (1999) apparent resistivities in the period range [15 days, 11 years], and Preliminary reference Earth model (PREM) densities and acoustic speeds are jointly inverted in the depth range [800 km, 2600 km] by using a Monte Carlo Markov Chain method. Given the uncertainties on these data, estimates of perovskite fraction are well constrained over the whole depth range, but information on temperature and iron content is only obtained for depths less than 2000 km, corresponding to the penetration depth of the long-period electromagnetic field. All parameter values are determined with an uncertainty better than 15–20% at the 1σ confidence level. The temperature in the uppermost lower mantle (i.e., down to 1300 km depth) is close to a value of 2200 K and increases along a superadiabatic gradient of 0.4 K km^{-1} between 1300 and 2000 km depth. Extrapolation of this gradient at greater depth leads to a temperature close to 2800 K at 2600 km depth. The iron content of the lower mantle is found to be almost constant and equal to 10–11% whatever the depth, while a significant linear decrease of the perovskite content is observed throughout the whole depth range, from 80% at 800 km depth down to ~65% at 2600 km depth.

Citation: Verhoeven, O., A. Mocquet, P. Vacher, A. Rivoldini, M. Menvielle, P.-A. Arrial, G. Choblet, P. Tarits, V. Dehant, and T. Van Hoolst (2009), Constraints on thermal state and composition of the Earth's lower mantle from electromagnetic impedances and seismic data, *J. Geophys. Res.*, *114*, B03302, doi:10.1029/2008JB005678.

1. Introduction

[2] Among the different geophysical methods of sounding the deep Earth, seismology provides the most reliable results. The two most popular one-dimensional radial seismic models Preliminary reference Earth model (PREM) [*Dziewonski and Anderson*, 1981] and ak135 [*Kennett et al.*, 1995] differ by less than 0.5% in the lower mantle. Radial seismic profiles of the Earth's mantle are classically used to give insight into its temperature and composition. Since the pioneer work by *Birch* [1952], experimental data on the elasticity of mantle minerals are used in the following way. First, values of density and elastic moduli, and their respective derivatives with respect to pressure and temperature, are tabulated for individual minerals at standard pressure and temperature conditions. Second, equations of state are used to extrapolate these parameters to conditions relevant to the deep mantle. Third, averaging procedures are used to compute seismic velocities of the mantle. The last two steps require a trial-and-error procedure to infer the temperature profile and composition of the mantle. The procedure is

[1]Royal Observatory of Belgium, Brussels, Belgium.
[2]Laboratoire de Planétologie et Géodynamique, UMR 6112, Université de Nantes, Nantes Atlantique Universités, CNRS, Nantes, France.
[3]Institut d'Astronomie et de Géophysique G. Lemaître, Université Catholique de Louvain, Louvain-la-Neuve, Belgium.
[4]LATMOS, IPSL, UMR, UVSQ 8639, Observatoire de Saint-Maur and Université Paris-Sud, CNRS, Saint Maur des Fossés, France.
[5]UEB, UBO, IUEM, Plouzané, France.

0148-0227/09/2008JB005678$09.00

constrained through the comparison between synthetic and observed values of densities and seismic velocities. Various equations of state exist (e.g., modified Birch-Murnaghan, Mie-Grüneisen [see *Jackson*, 1998]) and must be used with caution when extrapolating to lower mantle conditions, i.e., temperatures of the order of 2500 K, pressures up to 135 GPa [e.g., *Poirier*, 2000].

[3] The lower mantle represents the main part of the Earth's mantle, ranging from 670 to 2891 km depth. In this study, we focus on what may be the most homogeneous part of the lower mantle, which extends from 800 to 2600 km depth. The reason for starting at 800 km instead of 670 km is that we avoid the region where garnet is not totally changed into perovskite. We also avoid deliberately to consider the region 200–300 km above the mantle-core boundary, because it is complex and poorly constrained by geophysical data. This region, called the D″ layer, is characterized by a discontinuity in seismic waves, probably related to compositional or phase changes, such as the postperovskite transition [*Murakami et al.*, 2004].

[4] From the geochemical point of view, different models, such as the pyrolite model (see, e.g., *Green and Falloon* [1998] for a review) can describe the bulk mineralogical composition of the lower mantle. It is composed of 75 vol % Mg-perovskite, 5 vol % Ca-perovskite, and 20 vol % magnesiowüstite. *Deschamps and Trampert* [2004] tested a collection of mantle models against the density and elastic moduli of PREM. The originality of their study was to combine laboratory measurements and ab initio calculations to evaluate the elastic properties of the minerals. Although a pyrolite model with an adiabatic profile is compatible with their data, the perovskite fraction may drop as low as 65% at 2800 km depth. Depending on the modeling of the iron effect, the mean global iron fraction varies from 7.5% to 12% though its value may remain quite constant throughout the lower mantle. Using values of elastic constants obtained from laboratory measurements only, *Deschamps and Trampert* [2004] found that a superadiabatic profile was most likely. This conclusion was also obtained by *Cammarano et al.* [2005], who tested the compatibility of a pyrolite adiabatic mantle with seismic data. One of their major conclusions is that a pyrolite adiabatic model cannot fit the seismic data without a gradual physical or chemical change in the lower mantle that decreases the velocity gradient at depth. A superadiabatic temperature gradient seems a good candidate, as well as an increased iron content with depth. However, simultaneous measurements of compressional and shear wave velocities by *Li and Zhang* [2005] favor an adiabatic homogeneous lower mantle with a pyrolytic composition, although the results were obtained for an iron-poor lower mantle (iron number $x_{Fe} = 0.06$). *Mattern et al.* [2005] even support a subadiabatic profile. Although the composition found by Mattern et al. strongly depends on the a priori model, a total iron content of 0.10 ± 0.06 and a subadiabatic temperature gradient over most of the lower mantle range are features present in all their inversions of PREM and ak135 density and bulk sound velocity. The temperature profile obtained by *Mattern et al.* [2005] thus displays a thermal gradient at depth, that is opposite to the results of previous investigators.

[5] The incorporation of shear wave data in the inversion for thermal structure and chemical composition of the lower mantle leads to two kinds of models, depending on the not well-known value of the pressure derivative $\partial\mu/\partial P$ of the perovskite shear modulus [e.g., *Matas et al.*, 2007]. A value of the order of $\sim$1.8 does not match with the seismic properties of an adiabatic and chemically uniform lower mantle, but with a geotherm with large temperature gradients. This first kind of model predicts temperature values as high as 3400 K at the depth of 2700 km. The second kind of models, obtained with derivative $\partial\mu/\partial P \sim 1.6$, predicts lower values of the thermal gradient, and a temperature of the order of 2800 K at the depth of 2700 km.

[6] A major problem encountered in the inversion of seismic data is the trade-off between temperature, iron and compositional effects. *Matas et al.* [2007] developed a generalized inversion scheme enabling to evaluate the covariance between the parameters, and concluded that additional independent observables, such as electrical conductivity and anelastic properties, are necessary. Electrical conductivity and seismological data depend in a very different way on composition and on temperature. Such a unified study becomes now feasible because measurements of the electrical conductivity of individual minerals have been recently performed at high pressure and high temperature (see *Xu et al.* [2000] for a review).

[7] Conductivity profiles $\sigma(r)$ are deduced from the measured variations of the magnetic field originating from sources in the planetary ionized environment and in the core. The application of various assumptions and processing techniques to different data sets has resulted in different conductivity profiles because long-period induction data are scarce and the noise level may be high. In order to get rid of the assumptions inherent to the computation of the published conductivity profiles, we go back to electromagnetic impedances, which characterize the inductive response of the conductive mantle. Electromagnetic impedances studied by *Olsen* [1999] have been inverted by *Khan et al.* [2006], together with Earth's mass and mean moment of inertia, to investigate the temperature and the composition of the lower mantle. Their results favor a lower mantle geothermal gradient of $\sim$0.58 K km^{-1}, i.e., about twice the adiabatic gradient, and a pyrolitic composition. The inversion was performed in the period range 1 month to 1 year, and Khan et al. were forced to make strong prior assumptions on the parameterized geotherm and on the homogeneity of the lower mantle in terms of chemical composition.

[8] In this paper, we use both seismic (density and acoustic speed) and electromagnetic (apparent resistivity) data to study the internal structure of the Earth's lower mantle. These are processed data, in the sense that they are not directly recorded by geophysical instruments. In the following, we will use the word "data" to describe the input set to be inverted. First, we compute synthetic electromagnetic and seismic data from the parameters that govern the internal structure model, such as the perovskite fraction, the iron content, and the temperature, and we investigate the effect of each parameter on the geophysical data. Second, actual geophysical data are used in a stochastic inversion to infer the mineralogical composition and thermal state of the Earth's lower mantle.

[9] Section 2 is devoted to the presentation and discussion of the electromagnetic and seismic data that will be inverted in terms of internal structure. In section 3, we

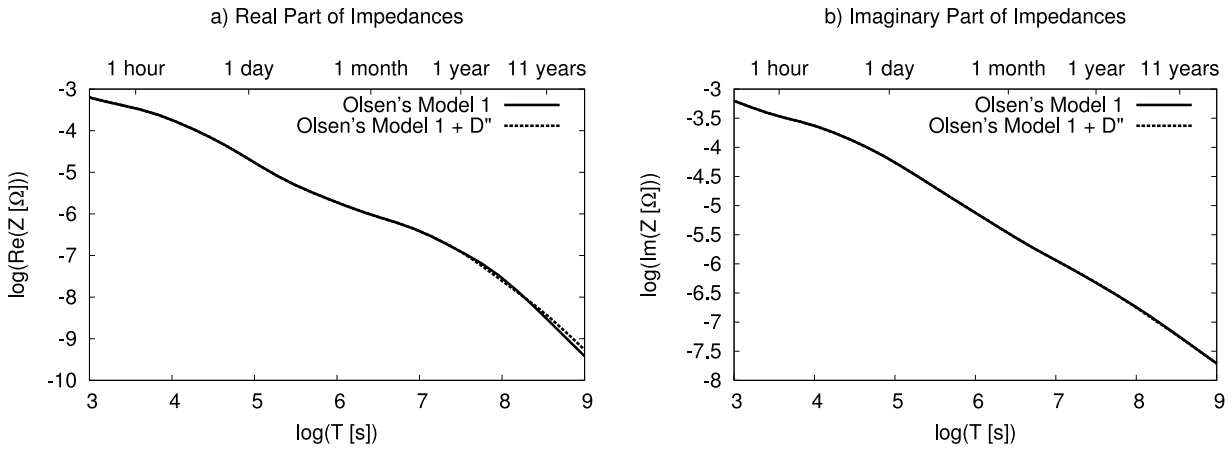

Figure 1. Effect of the electrical conductivity of the D″ layer on the computation of EM impedances. The (a) real and (b) imaginary parts of the electromagnetic impedances corresponding to the electrical conductivity of *Olsen*'s [1999] model 1 (solid curve) as a function of the logarithm of the period *T*. The dashed curve represents the same computation supplemented with a D″ layer of 200 km thickness and with a conductivity of 10^3 S m^{-1}.

compute synthetic geophysical data for a homogeneous pyrolytic adiabatic lower mantle (the forward problem). Elastic and electrical properties of the minerals are reviewed. We further discuss the effect of each parameter on the whole data set. In section 4, we present the Bayesian framework of the stochastic inversion and perform the inversion of synthetic data. In section 5, observed geophysical data are inverted and interpreted in terms of temperature and composition of the lower mantle.

2. Geophysical Data and Their Uncertainties

2.1. Electromagnetic Data

[10] The interaction between a time-variable electromagnetic wave and a conductive medium results in induced electric currents, which tend to oppose its penetration in the conductive medium. The induced magnetic field is characterized by its vertical scale factor, which is equal to $\sqrt{1/\mu_0\sigma\omega}$, where μ_0 is the magnetic permeability of the vacuum, σ is the electrical conductivity of the medium and ω is the pulsation of the electromagnetic field. The complex impedance Z characterizes the inductive response of the conductive planet to the external magnetic field. This field has energy over a wide period range [see, e.g., *Banks*, 1969]: the lowest periods (up to a few days) enable one to probe the crust and upper mantle, and with longer periods (up to a few years), one can probe the lower mantle down to about 1500 km depth. Investigation beyond that depth requires to use periods as long as 11 years (solar cycle).

[11] Our objective is to use a set of electromagnetic impedances that can be interpreted in terms of lower mantle conductivity only. Since impedances depend on the conductivity distribution in the whole Earth, we have to avoid existing contaminations associated with oceans, possible shallow (less than 400 km) heterogeneities, and the conductive D″ layer. Such identification governs the choice of the period range of the electromagnetic impedances.

[12] First, consider the case of the oceans. The electrical conductivity of seawater is higher than that of the lithospheric materials by more than 1 order of magnitude and even more for most of them. The resulting sharp conductivity contrast between continents and oceans is the origin of the so-called coast effect [see, e.g., *Menvielle et al.*, 1982; *Semenov and Jozwiak*, 2006]. In order to get rid of the coast effect on the impedance, we restrict the period range to exclude periods for which this effect becomes important. As computed by *Tarits* [1994], the coast effect becomes negligible for periods longer than 10–15 days.

[13] Second, let us consider the effect of highly conductive bodies in the upper mantle on the computation of impedances. *Tarits* [1994] modeled the dipping slabs of subduction zones by patches of conductivity 1 order of magnitude higher than the conductivity of the surrounding upper mantle. He showed that such level of heterogeneity affects the real part of electromagnetic impedances Z(T) in the period range [10^3 s, 10^8 s], but that the imaginary part is only marginally affected for periods longer than 5 days. Since the imaginary part is at least three times greater than the real part, working with the apparent resistivity, proportional to the square modulus of impedance, enables us to minimize the effect of lateral heterogeneities on the value of electromagnetic impedances at periods longer than 5 days. We checked the influence of the upper layer (0 < depth < 800 km) conductivity on the results computed at depths greater than 800 km depth by comparing the results obtained with two different choices for the upper layer conductivity that differ by 1 order of magnitude (0.1 and 1 S m^{-1}). The results, not presented in the paper, show that in the period range chosen in the paper, this upper layer conductivity does not affect the square modulus of the impedances. This ensures that our results for the lower mantle are not influenced by the electrical properties of the transition zone.

[14] Third, we define a boundary condition for the conductivity at the bottom of the investigated region (2600 km). Little is known about the conductivity of the D″ layer but its conductance (the conductivity-thickness product for a homogeneous layer) can be constrained by the observation of the mantle filtering of the core-generated field [see, e.g., *Mandea*

Table 1. *Olsen* [1999] Electromagnetic Data Considered in This Study[a]

T (s)	C (km)	$\Delta\|C\|$ (km)	Z (Ω)	log $\rho_a(T)$
346,896,000	2180 – 126 i	480	$2.868 \times 10^{-9} + 4.962 \times 10^{-8}$ i	−0.9644
31,536,000	1592 – 232 i	64	$5.809 \times 10^{-8} + 3.986 \times 10^{-7}$ i	−0.1884
15,768,000	1200 – 420 i	112	$2.103 \times 10^{-7} + 6.009 \times 10^{-7}$ i	−0.0918
10,512,000	1517 – 473 i	98	$3.553 \times 10^{-7} + 1.139 \times 10^{-6}$ i	0.2780
6,307,200	1292 – 436 i	67	$5.458 \times 10^{-7} + 1.617 \times 10^{-6}$ i	0.3669
3,942,000	1085 – 376 i	73	$7.531 \times 10^{-7} + 2.173 \times 10^{-6}$ i	0.4218
2,866,909	1019 – 397 i	66	$1.093 \times 10^{-6} + 2.806 \times 10^{-6}$ i	0.5177
2,592,000	999 – 292 i	22	$8.895 \times 10^{-7} + 3.043 \times 10^{-6}$ i	0.5185
2,102,400	976 – 291 i	60	$1.093 \times 10^{-6} + 3.665 \times 10^{-6}$ i	0.5906
1,296,000	938 – 308 i	20	$1.876 \times 10^{-6} + 5.715 \times 10^{-6}$ i	0.7737

[a]C function is related to the complex impedances Z by the relation $Z(T) = i\mu 2\pi C(T)/T$, where μ is the magnetic permeability. Apparent reactivities $\rho_a(T)$ are computed from the impedances using the formula $\rho_a(T) = (T/2\pi\mu_0)\,|Z(T)|^2$.

et al., 1999], studies of decadal length-of-day variations [e.g., *Holme*, 1998] and nutation [e.g., *Buffett et al.*, 2002]. These studies suggest the presence of a thin conducting layer at the base of the mantle with a conductivity of the order of 10^2–10^3 S m^{-1}. The effect of the D″ conductivity is assessed using model 1 of *Olsen* [1999] in the period range [10^3 s, 10^8 s]. Figures 1a and 1b display the real and imaginary parts, respectively, of the impedances computed for the model with and without a D″ layer of conductivity equal to 10^3 S m^{-1}. There is no noticeable effect of the D″ conductivity on the imaginary part of the impedances, and the two sets differ by a few $10^{-10}\Omega$ for the longest periods of 11 years (or $10^{8.54}$ s, the longest period at which impedance estimates are available). This difference is smaller than the errors on experimental data [see, e.g., *Olsen*, 1999]. In the subsequent computation of impedances, we consider a D″ layer with a conductivity of 10^3 S m^{-1}.

[15] According to the previous discussion, we characterize the electromagnetic properties of the lower mantle by using the apparent resistivity ρ_a at periods longer than 15 days and shorter than or equal to 11 years, the longest period related to external source induction. At periods longer than 11 years, the core field, attenuated by the mantle filter, dominates the signal recorded at the surface [*Currie*, 1968].

[16] The impedances published by *Olsen* [1999] were derived from typically 50 years of three-component magnetic variations measured at a worldwide network of 42 observatories (see Table 1). The choice of considering electromagnetic impedances instead of electrical conductivity profile is due to the nonunicity of the computation of the σ profile from the few noisy impedance data available. Indeed, the ten periods of interest isolated in the electromagnetic data (Table 1) provide a small number of impedances, which only poorly constrain the lowest region of the mantle. This is best evidenced by the three σ profiles proposed by *Olsen* [1999], corresponding to the same set of impedances. Two models, differing by more than half an order of magnitude in conductivity values, share the same misfit to the data. The third model, with conductivities of the order of 10 S m^{-1} at the base of the lower mantle (i.e., more than 1 order of magnitude lower than the two other models) has a higher misfit. The inversion of the impedances in terms of σ profiles needs additional assumptions, usually on the smoothness of the profile.We prefer not to use such assumptions, and invert the electromagnetic impedances, instead of the σ profile, in terms of temperature and composition of the lower mantle.

2.2. Seismological Data

[17] As the seismic equivalent to the electromagnetic impedances, we consider the radial seismic models such as PREM [*Dziewonski and Anderson*, 1981]. Both data sets are derived from a large number of observations: electromagnetic impedances are computed from magnetic field measurements recorded at a network of magnetic observatories, and the PREM seismic velocity and density radial profiles are derived from the analysis of about 900 normal modes, 2,000,000 P wave arrival times, and 250,000 S wave arrival times, recorded at least 30 seismic stations [*Dziewonski and Anderson*, 1981]. Although magnetic field variations and seismic arrival times are for a three-dimensional Earth, the derived electromagnetic impedances and seismic velocities are considered as our best estimates of a representative one-dimensional model of the Earth since they result from the joint analysis of a large number of data.

[18] We only use the acoustic wave speed instead of v_P and v_S seismic velocities because of the limited number of experimental data on the shear modulus of mantle phases, and because of a possible inconsistency between ab initio and experimental data for the shear modulus of Mg-perovskite [*Deschamps and Trampert*, 2004] and for its pressure derivative [*Matas et al.*, 2007]. Furthermore, the modeling of S wave velocities requires to include anelastic effects [see, e.g., *Cammarano et al.*, 2005], which are not well known for lower mantle phases. These effects are negligible for the bulk modulus and so also for acoustic wave speeds.

[19] In comparison with electromagnetic data, globally averaged seismic data (i.e., travel times and normal modes) are less affected by deep lateral heterogeneities (anomalies of a few percent). As a result, spherically symmetric seismic models of the Earth, such as PREM, are very well determined with little uncertainty. *Mattern et al.* [2005] considered that PREM densities and bulk sound velocities have uncertainties of 0.5% and 0.1%, respectively. Since PREM bulk sound velocities differ from ak135 velocities [*Kennett et al.*, 1995] by less than 0.5%, we consider conservative uncertainties of 1% and 0.5% on density and bulk acoustic velocity values, respectively.

3. Forward Problem

[20] This section describes the computation of synthetic geophysical data. First, we explain our modeling hypothesis and define the model in terms of parameters and data. Second, we describe the computation of synthetic data from the parameter values. In each subsection, the details of the

Table 2. List of Laboratory Results Concerning Elastic Properties of Mineral i[a]

Mineral	$\rho_0^{(i)}$ (10^3 kg m^{-3})	$\rho_{0,Fe}^{(i)}$ (10^3 kg m^{-3})	$K_{S_0}^{(i)}$ (GPa)	$\left.\frac{\partial K_S^{(i)}}{\partial P}\right\|_0$	$\left.\frac{\partial K_S^{(i)}}{\partial T}\right\|_0$ (GPa K^{-1})	$\gamma_{th_0}^{(i)}$	$q^{(i)}$	$a_0^{(i)}$ (10^{-5} K^{-1})	$b_0^{(i)}$ (10^{-8} K^{-2})
Mg-perovskite	4.110[b]	1.085[b]	253(2)[c]	4.4(1)[c]	−0.021(2)[c]	1.84(2)[d]	1.69(3)[d]	2.461(119)[e]	0.165[e]
Mg-wüstite	3.583[e]	2.277[e]	162(1)[f,g]	3.8(1)[e]	−0.021(4)[h]	1.63(2)[f]	0.54(3)[f]	3.78(12)[f]	0.74(13)[f]

[a]The $\rho_0^{(i)}$ and $K_{S_0}^{(i)}$ refer to the density and to the bulk modulus of the ith mineral at STP conditions (STP, $P_0 = 10^5$ Pa, $T_0 = 298$ K). $(\partial K_S^{(i)}/\partial P)|_0$ and $(\partial K_S^{(i)}/\partial T)|_0$ denote the derivatives, at STP conditions, of the bulk modulus of the ith mineral with respect to pressure P and temperature T, respectively; $\rho_{0,Fe}^{(i)}$ gives the iron content dependence of the density. The coefficients $a_0^{(i)}$ and $b_0^{(i)}$ govern the polynomial expression of the thermal expansion α; $\gamma_{th_0}^{(i)}$ is the value of Grüneisen's parameter at STP conditions. Numbers in parentheses are experimental errors (last digits).
[b]*Fiquet et al.* [1998]. See *Mattern et al.* [2005] for iron dependence estimation.
[c]*Li and Zhang* [2005].
[d]*Gong et al.* [2004].
[e]From the analysis of *Mattern et al.* [2005].
[f]*Van Westrenen et al.* [2005].
[g]*Jacobsen et al.* [2002].
[h]From the compilation of *Cammarano et al.* [2003].

computation are followed by a review of the presently available experimental results on the elastic and electrical properties of minerals at the lower mantle thermodynamical conditions. Third, we discuss the sensitivity of the data to each parameter.

3.1. Modeling Hypothesis, Parameters, and Data

[21] In the present study, we do not consider Ca-perovskite as part of the lower mantle composition since its effects on density and elastic moduli are of second-order compared to other compositional parameters [*Deschamps and Trampert*, 2004; *Li and Zhang*, 2005]. This restriction might slightly affect the computation of the electrical conductivity of the lower mantle although there is no experimental evidence, to the best of our knowledge, for a noticeably different conductivity between Ca-perovskite and Mg-perovskite. Therefore, we represent the lower mantle composition as a binary mixture of Mg-perovskite and magnesiowüstite. The fraction of perovskite with respect to magnesiowüstite is allowed to vary with depth.

[22] We assume that iron is partitioned equally between perovskite and magnesiowüstite. Although experimental results show that Fe preferentially partitions into magnesiowüstite rather than into perovskite [see, e.g., *Mattern et al.*, 2005, and references therein], the effect of this partitioning is negligible on the computation of synthetic wave speeds and density [*Li and Zhang*, 2005; *Mattern et al.*, 2005]. The effect of iron on the electrical conductivity of perovskite has, to the best of our knowledge, never been measured. Any modeling of the electrical conductivity of the lower mantle with unequal iron partitioning between perovskite and magnesiowüstite is therefore premature. Unequal iron partitioning would affect our results only if the effect of iron on the electrical conductivity of magnesiowüstite were very different from the effect on perovskite. However, *Vacher and Verhoeven* [2007] showed that the effect of iron on the electrical conductivity of magnesiowüstite [*Dobson and Brodholt*, 2000] is close to the perovskite/magnesiowüstite assemblage [*Poirier and Peyronneau*, 1992].

[23] Our model of the lower mantle consists of three quantities: (1) the temperature profile $T(r)$, (2) the volume fraction of perovskite $X_{pv}(r)$, and (3) the iron number $x_{Fe}(r)$ = Fe/(Fe + Mg), where Fe and Mg indicate the bulk molar abundances, respectively. These parameters determine, via the forward problem, the following data: (1) the acoustic wave speed $v_\phi(r)$ at radius r, (2) the density $\rho(r)$ at radius r, and (3) the apparent resistivity $\rho_a(T) = (T/2\pi\mu_0)|Z(T)|^2$, where $Z(T)$ is the electromagnetic impedance at period T and μ is the magnetic permeability.

[24] To compute these data from the parameter values, we also use the pressure profile of PREM [*Dziewonski and Anderson*, 1981] in the Earth' s lower mantle. The model extends from 800 to 2600 km depth. It is divided into 50 layers of equal thickness.

3.2. Computation of Geophysical Data

[25] We compute synthetic values of bulk sound velocity $v_\phi(r)$, density $\rho(r)$, and apparent resistivities $\rho_a(T)$ from the parameters $T(r)$, $X_{pv}(r)$, and $x_{Fe}(r)$, using laboratory measurements of the electrical and elastic properties of perovskite and magnesiowüstite. We adopt the most recent values of the elastic and electrical properties of lower mantle minerals obtained from high-pressure and high-temperature experiments.

[26] The experimental values at standard temperature and pressure (STP, $P = 10^5$ Pa, $T = 298$ K) of the constants are listed in Tables 2 and 3 for the elastic and electrical properties of Earth's lower mantle phases, respectively. We denote STP values by the subscript 0, unless stated otherwise.

3.2.1. Density and Acoustic Wave Speed

[27] For the calculations of the density and acoustic wave speed of a perovskite-magnesiowüstite assemblage in the lower mantle, we adapt the method described by *Verhoeven et al.* [2005] for the Martian mantle.

[28] In step 1, for given $T(r)$, $X_{pv}(r)$, and $x_{Fe}(r)$, compute the volume fraction of magnesiowüstite $X_{mw}(r) = 1 - X_{pv}(r)$ for each layer. As no iron partitioning between perovskite and magnesiowüstite is considered in this study, the iron fraction $y^{pv}(r)$ and $y^{mw}(r)$ of perovskite and magnesiowüstite are equal, for each layer, to the iron number $x_{Fe}(r)$.

[29] In step 2, compute STP densities of iron-bearing minerals: $\rho_0^{(i)} + y^{(i)}\,\rho_{0,Fe}^{(i)}$, where $\rho_{0,Fe}^{(i)}$ denotes the increase of density due to iron substitution (see Table 2) and the index i refers to the two mineral phases considered here: perovskite and magnesiowüstite.

[30] In step 3, use an iterative procedure of isobaric heating followed by adiabatic compression to calculate the values of density $\rho^{(i)}(r)$ and bulk modulus $K^{(i)}(r)$ of each mineral (i) as a function of $T(r)$ and $P(r)$ (see *Verhoeven et al.* [2005] for details). For the sake of simplicity, the mineral

Table 3. List of Constants Needed for the Computation of the Electrical Conductivity as a Function of Temperature and Iron Content[a]

Mineral	$\log \sigma^{(i)}_{0;\,ref}$	$E^{(i)}_{0;\,ref}$ (eV)	$\alpha^{(i)}$	$\beta^{(i)}$ (eV)	$\Delta V^{(i)}$ (cm^3 mol^{-1})
Mg-perovskite	2.03(11)[b,c]	0.76(4)[b,c]	3.56(132)[d]	−1.72(38)[d]	−0.26(3)[e]
Mg-wüstite	2.56(10)[b,e]	0.88(3)[b,e]	3.14(7)[e]	0.[e]	−0.26(69)[e]

[a]See equations (14) and (15). For each mineral i, $\sigma^{(i)}_{0;\,\mathrm{ref}}$ and $E^{(i)}_{0;\,\mathrm{ref}}$ represent the preexponential factor and the activation energy, respectively, for an iron fraction y equal to 0.1 (i.e., Mg # = 0.9), for atmospheric pressure and temperature which tends to infinity. The constants $\alpha^{(i)}$ and $\beta^{(i)}$ govern the iron content contribution to the preexponential factor and to the activation energy, respectively. $\Delta V^{(i)}$ is the activation volume for mineral i. Numbers in parentheses are experimental errors (last digits).
[b]*Xu et al.* [2000].
[c]*Shankland et al.* [1993].
[d]The constants α and β are identical to pv/mw assemblage values computed from the work by *Poirier and Peyronneau* [1992].
[e]*Dobson and Brodholt* [2000].

index (i) is omitted in the description of the following procedure:

[31] In step 3.1, take an approximate value for the potential temperature ϑ, defined as the temperature at P_0 that would lead to the given temperature $T(r)$ and pressure $P(r)$ along an adiabatic path.

[32] In step 3.2, heat mineral i at constant pressure P_0 from T_0 to ϑ. Density is computed using an empirical linear law [*Saxena and Shen*, 1992] $\alpha(P_0,T) = a_0 + b_0 T$ (Table 2) to describe the variation of the thermal expansivity $\alpha(P_0,T)$ with temperature,

$$\rho(P_0,\vartheta) = \rho_0 \exp\left[a_0(T_0-\vartheta) + \frac{b_0}{2}\left(T_0^2-\vartheta^2\right)\right] \tag{1}$$

The value of the adiabatic bulk modulus $K_S(P_0,\ \vartheta)$ is computed at constant P_0 using the formula

$$K_S(P_0,\vartheta) = K_{S_0}\left(\frac{\rho(P_0,\vartheta)}{\rho_0}\right)^{\delta_{S_0}} \tag{2}$$

where δ_{S_0} is the Anderson-Grüneisen parameter, defined by $\delta_{S_0} = -(1/\alpha_0)(\partial \ln K_S/\partial T)_{P_0}$. The value of the Anderson-Grüneisen parameter can be considered as independent of temperature [*Anderson*, 1988]. It is therefore only computed at STP conditions for each mineral.

[33] In step 3.3, compress adiabatically the mineral from (P_0, ϑ) conditions to (P, T) conditions. To avoid using weakly constrained values of the second derivative of K_S with respect to pressure, we use the third-order Birch-Murnaghan equation of state [e.g., *Trampert et al.*, 2001]:

$$P(r) = -3\,K_S(1-2\varepsilon)^{5/2}\left\{\varepsilon + \frac{3}{2}\left[4-\left(\frac{\partial K_S}{\partial P}\right)\right]\varepsilon^2\right\} \tag{3}$$

where

$$\varepsilon = \frac{1}{2}\left\{1-\left[\frac{\rho(P,T)}{\rho(P_0,\vartheta)}\right]^{2/3}\right\} \tag{4}$$

is the Eulerian strain of the mineral under adiabatic compression. The value of the local density $\rho(P(r),\ T(r))$ is then obtained by computing the unique negative real root of equation (3). Similarly K_S is computed as

$$K_S(r) = K_S(1-2\varepsilon)^{5/2} \cdot \left\{1+\left[5-3\left(\frac{\partial K_S}{\partial P}\right)\right]\varepsilon - \frac{27}{2}\left[4-\left(\frac{\partial K_S}{\partial P}\right)\right]\varepsilon^2\right\} \tag{5}$$

In equations (3) and (5), all quantities are evaluated at (P_0, ϑ) conditions. Since the second mixed derivative $\partial^2 K_S/\partial T \partial P$ is poorly constrained by laboratory measurements, we assume, following *Jackson* [1998], that $\partial K_S/\partial P$ is temperature-independent at ambient pressure, namely

$$\left(\frac{\partial K_S}{\partial P}\right)_{(P_0,\vartheta)} \approx \left(\frac{\partial K_S}{\partial P}\right)_{(P_0,T_0)} \tag{6}$$

[34] In step 3.4, the temperature along an adiabatic compression path is given by

$$T = \vartheta \exp\left\{\frac{\gamma_{th_0}}{q}\left[\frac{\rho_0}{\rho(P_0,\vartheta)}\right]^q\left[1-\left(\frac{\rho(P_0,\vartheta)}{\rho(P,T)}\right)^q\right]\right\} \tag{7}$$

where γ_{th} is Grüneisen parameter and where we used the quasi-harmonic approximation

$$\gamma_{th}(P,T)\rho(P,T)^q = \text{const.} \tag{8}$$

The constant q depends on the mineral considered (see Table 2). By comparing the result of equation (7) with the value of $T(r)$, we tune the value of the temperature ϑ and go to step 3.1 until this identity is obtained within an error of 5 K.

[35] In step 4, compute the density $\rho(r)$ of the assemblage at depth r as the arithmetic mean of individual densities $\rho^{(i)}(r)$ weighted by their volume fraction $X^{(i)}$. The bulk modulus $K(r)$ is computed from the individual values $K^{(i)}(r)$ using the procedure of *Hashin and Shtrikman* [1963].

[36] In step 5, from the values of $\rho(r)$ and $K_S(r)$, compute the acoustic wave speed profile $v_\phi(r)$ as

$$v_\phi(r) = \sqrt{\frac{K_S(r)}{\rho(r)}} \tag{9}$$

[37] Many papers have reviewed available elastic data of lower mantle minerals [e.g., *Cammarano et al.*, 2003; *Deschamps and Trampert*, 2004; *Mattern et al.*, 2005; *Stixrude and Lithgow-Bertelloni*, 2005]. However, several new experimental results have been obtained since these reviews were published, and we therefore briefly review the available data.

[38] For perovskite, recent high-pressure/high-temperature experiments have provided values of the bulk modulus K_S in the range [250 GPa, 260 GPa] [e.g., *Fiquet et al.*, 2000; *Gong et al.*, 2004; *Sinogeikin et al.*, 2004; *Li and Zhang*,

2005]. *Li and Zhang* [2005] performed experiments on a polycrystalline sample of pure $MgSiO_3$, using ultrasonic interferometry in conjunction with X-ray diffraction. They use a new procedure to derive values of elastic moduli and of their derivatives that is independent of the pressure determination. Their values are used here. It should be noted that they give an unusually high value for dK_S/dP, 4.4, while all previous studies fixed the value to 4.0. Values of thermal expansion coefficients and temperature derivative of the bulk modulus are also given by *Li and Zhang* [2005]. However, their experiments are restricted to moderate temperatures (less than 873 K) and we prefer therefore the values found by *Mattern et al.* [2005], based on inversions of all available P-V-T data. Their inversion made with $K_T = 250$ GPa is consistent with the results of *Li and Zhang* [2005]. As reported by recent studies [e.g., *Kiefer et al.*, 2002; *Li and Zhang*, 2005], the bulk modulus of perovskite is only marginally affected by a variation of iron content.

[39] For magnesiowüstite, *Van Westrenen et al.* [2005] studied a $(Mg_{0.64}Fe_{0.36})O$ sample with in situ X-ray diffraction up to 26.7 GPa and 2173 K. They found values for P-T derivatives of the bulk modulus and thermal expansion similar to that of the pure Mg end-member. These values result from a fit of both their new data and data reported by others. Their data are therefore used here. The bulk modulus is fixed to 162(±1) GPa, from the recent studies of *Jacobsen et al.* [2002] and *Van Westrenen et al.* [2005]. For iron content values relevant to the Earth's lower mantle (i.e., less than 0.3), the latter study suggests that the bulk modulus is independent of the iron content.

[40] The relative uncertainties affecting the elastic constants are listed in Table 2. All are less than 10%, except for the temperature derivative of the bulk modulus and for the b_0 coefficient of thermal expansion, which are roughly equal to 20% for magnesiowüstite.

3.2.2. Electromagnetic Impedances

[41] To calculate period-dependent impedances, we first determine, for the lower mantle mineralogy, the conductivity profile, and we solve the electromagnetic 1-D induction problem for a multilayered sphere [see, e.g., *Srivastava*, 1966]. Impedances are computed for periods in the range [15 days, 11 years]. The magnetic field is solution of the Maxwell equations and is derived, at a given frequency ω, from a single magnetic potential $P(r, \omega)$ which is a solution of the Helmholtz equation

$$\nabla^2 P(r,\omega) = k^2 P(r,\omega) \tag{10}$$

where $k = \sqrt{i\omega\mu_0\sigma}$ is the induction number, σ is the electrical conductivity, and r is the radius. In each layer, the solution is of the form

$$P(r,\omega) = A\, j_1(kr) + B\, n_1(kr), \tag{11}$$

where the functions j_1 and n_1 are the spherical Bessel functions of the first and second kinds, respectively. The constants A and B are found by applying the boundary conditions of continuity for P and $\partial_r P$ at each layer interface. The electromagnetic impedance $Z(\omega = 2\pi/\mathrm{T})$ is equal to

$$Z(\omega) = i\omega\mu r \frac{P(r,\omega)}{\partial_r P(r,\omega)} \tag{12}$$

where $Z(\omega)$ is evaluated at $r = 6371$ km, the mean radius of the Earth. To compute impedances, we therefore need the electrical conductivity of the crust, upper mantle and core. In the following calculations, the conductivity of the upper mantle and crust is fixed to 10^{-1} S m^{-1} [*Olsen*, 1999] and the conductivity of the core is equal to 10^5 S m^{-1} [*Stacey and Loper*, 2007].

[42] The electrical conductivity $\sigma(r)$ of the perovskite/magnesiowüstite assemblage at radius r is computed from the individual mineral values $\sigma^{(i)}(r)$ using the procedure of *Hashin and Shtrikman* [1962]. For each mineral (i), the electrical conductivity $\sigma^{(i)}(r)$ is a function of $T(r)$, $P(r)$ and iron fraction $y^{(i)}(r)$:

$$\sigma^{(i)}\left(T,P,y^{(i)}\right) = \sigma_0^{(i)}\left(y^{(i)}\right)\ \exp\left[-\frac{E_0^{(i)}\left(y^{(i)}\right) + P\Delta V^{(i)}}{kT}\right] \tag{13}$$

where $E_0^{(i)}$ and $\sigma_0^{(i)}$ are the activation energy and the preexponential factor, respectively, $\Delta V^{(i)}$ is the activation volume, and k is Boltzmann's constant.

[43] The electrical conductivity of various iron-bearing minerals (olivine, pyroxene, magnesiowüstite and perovskite/magnesiowüstite assemblage) can be expressed according to the empirical equations [*Vacher and Verhoeven*, 2007]:

$$\log\left(\sigma_0^{(i)}\left(y^{(i)}\right)\right) = \log\left(\sigma_{0;\,\mathrm{ref}}^{(i)}\right) + \alpha^{(i)}\log\left(\frac{y^{(i)}}{y_{\mathrm{ref}}}\right) \tag{14}$$

$$E_0^{(i)}\left(y^{(i)}\right) = E_{0;\,\mathrm{ref}}^{(i)} + \beta^{(i)}\left(y^{(i)} - y_{\mathrm{ref}}\right) \tag{15}$$

In these equations, $\sigma_{0;\,\mathrm{ref}}^{(i)}$ is the value of the electrical conductivity in the limit that the temperature goes to infinity, and the iron fraction is equal to y_{ref}; $E_{0;\,\mathrm{ref}}^{(i)}$ is the activation energy for an iron fraction equal to y_{ref}. This reference iron fraction y_{ref} is set to 0.1, which is the most frequently used value for iron-bearing samples. The constants $\alpha^{(i)}$ and $\beta^{(i)}$ govern the iron content contribution to the preexponential factor and to the activation energy, respectively. The values of the constants entering equations (14) and (15) (Table 3) are calculated for each mineral using the two-step procedure detailed by *Vacher and Verhoeven* [2007]. First, only the contribution of iron (α and β coefficients) is derived from studies with iron bearing samples [*Poirier and Peyronneau*, 1992; *Dobson and Brodholt*, 2000]. Second, reference values of $\log(\sigma_0)$ and E_0 are computed from the review of *Xu et al.* [2000] for $y = 0.1$. This grounds formulas (13), (14), and (15) on samples with iron content close to 10% and prevents variations coming from different experimental conditions.

3.3. Sensitivity of Geophysical Data to Changes in Parameter Values

[44] In this section, we compute synthetic profiles for the density, acoustic wave speed, electrical conductivity and their corresponding apparent resistivities in the period range [15 days, 11 years], and we study the sensitivity of these synthetic data to each parameter. We consider a reference model of pyrolite composition (without Ca-perovskite), i.e.,

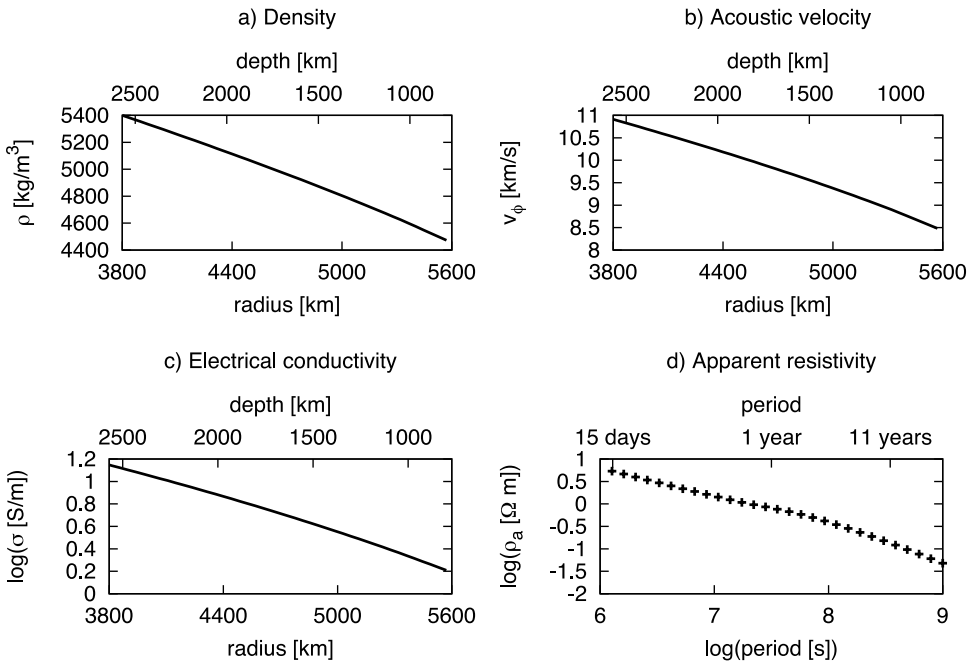

Figure 2. Reference synthetic data: (a) density, (b) acoustic wave speed, (c) electrical conductivity, and (d) apparent resistivities. Data computed for X_{pv} = 80%, a potential temperature of 1600 K, an adiabatic gradient of 0.3 K km^{-1}, and a constant iron content equal to 10%.

$X_{pv}(r)$ = 80% for all r. The temperature gradient is assumed to be constant, equal to 0.3 K km^{-1} (close to adiabatic) with a potential temperature (i.e., adiabatic temperature extrapolated to the surface) equal to 1600 K. This latter value is constrained by the pressure-temperature boundaries of the mineralogical transformation ringwoodite → perovskite + magnesiowüstite, which is responsible for the seismic discontinuity at 670 km depth [see, e.g., *Poirier*, 2000]. The iron number $x_{Fe}(r)$ is assumed constant throughout the whole lower mantle and is set to 10% (see Figure 2). In order to study the range of possible solutions and to gain some insight into the effect of each parameter, we vary in turn, the values of the perovskite content, the temperature and the iron number. The variations of the parameter values are chosen to cover the range of values that seem reasonable for the Earth's lower mantle.

3.3.1. Perovskite Content

[45] Figure 3 shows the effect on the synthetic data of a change of the perovskite fraction from 80% to 50% and 100%. This range includes all perovskite fractions resulting from the latest inversions of PREM [*Deschamps and Trampert*, 2004; *Mattern et al.*, 2005; *Matas et al.*, 2007]. Both density and acoustic speed increase with increasing perovskite content, although the density variation vanishes at a depth of about 2500 km. The acoustic speed variation remains constant throughout the whole lower mantle. At lower mantle temperatures and for an iron content equal to 10%, the electrical conductivity of magnesiowüstite is slightly larger than that of perovskite [*Xu et al.*, 2000]. Therefore, increasing the perovskite content decreases the electrical conductivity of the assemblage. As can be seen from Figure 3c, a decrease of log(σ) of 0.15 log units is obtained when X_{pv} increases from 50% to 100%. This decrease is almost constant over the whole depth range since we use an adiabatic temperature profile and an identical effect of pressure for both minerals, due to the same value of activation volume for both minerals (see Table 3) [*Shankland et al.*, 1993; *Dobson and Brodholt*, 2000]. The very small decrease of the conductivity with perovskite content induces at most a 0.1 log unit variation of the apparent resistivity value at short periods (Figure 3d). At periods longer than 11 years, the core conductivity dominates the resistivity signal. Among the three sets of data, acoustic velocity is the most sensitive to perovskite content, increasing by 0.8 km s^{-1} on average as the perovskite fraction increases from 50% to 100%.

3.3.2. Temperature

[46] Figure 4 shows the effect of variations in the temperature gradient and in the potential temperature. For a fixed temperature gradient of 0.3 K km^{-1}, we compute synthetic data for potential temperatures equal to 1400 and 2000 K. We also fix the potential temperature at 1600 K and consider extreme values for constant temperature gradient equal to 0.2 and 0.7 K km^{-1}. The density and the acoustic wave velocity are only marginally dependent on the temperature (see Figures 4a and 4b). The maximum differences in their values are less than 1%. Lower mantle temperature is therefore poorly resolved with inversions based on acoustic wave velocity and density only. An improvement of the resolution requires using shear wave velocities [e.g., *Deschamps and Trampert*, 2004; *Cammarano et al.*, 2003], but they suffer from large uncertainties on the pressure derivative of the shear modulus, in particular perovskite [*Matas et al.*, 2007], and from our poor knowledge of the anelastic contributions to the temperature dependence of shear wave velocities at pressures relevant to the lower mantle [*Matas and Bukowinski*, 2007].

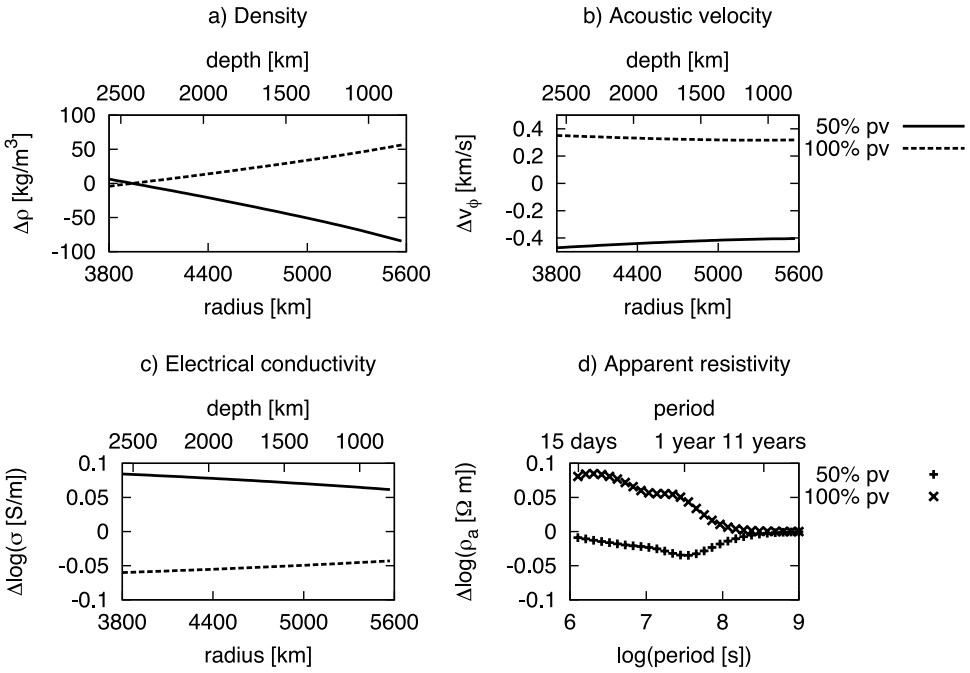

Figure 3. Effect of perovskite content on (a) the computation of lower mantle density, (b) acoustic wave speed, (c) electrical conductivity, and (d) apparent resistivity. Variations of geophysical data are computed for X_{pv} = 50% and 100% and compared to the reference values at X_{pv} = 80% (see Figure 2).

[47] The electrical conductivity has the strongest temperature dependence, with a maximum difference between the profiles of about 0.6 log unit and 0.4 log unit at the top and at the bottom of the model, respectively (see Figure 4c). Increasing the temperature results in a decrease of the apparent resistivities in most of the period range. The effect is particularly noticeable at long periods relevant to the lower mantle, i.e., around 1 year (see Figure 4d). The

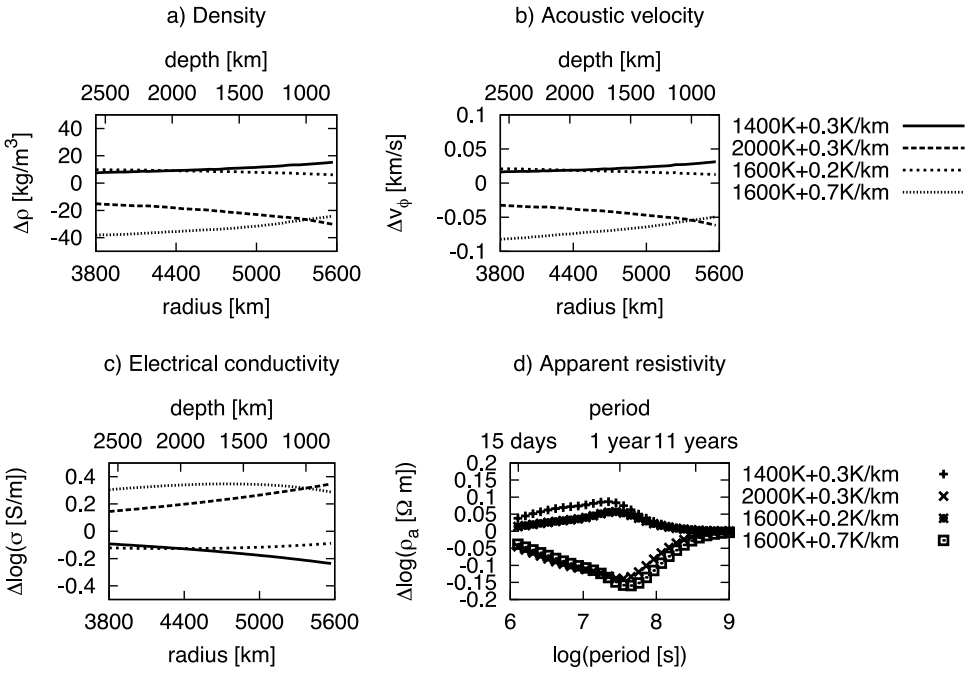

Figure 4. Effect of temperature on (a) the computation of lower mantle density, (b) acoustic wave speed, (c) electrical conductivity, and (d) apparent resistivity. Variations of geophysical data are computed for a temperature gradient equal to 0.2 and 0.7 K km^{-1} with a potential temperature of 1600 K and with a gradient of 0.3 K km^{-1} with a potential temperature of 1400 and 2000 K. Data variations are computed relative to the reference values displayed in Figure 2.

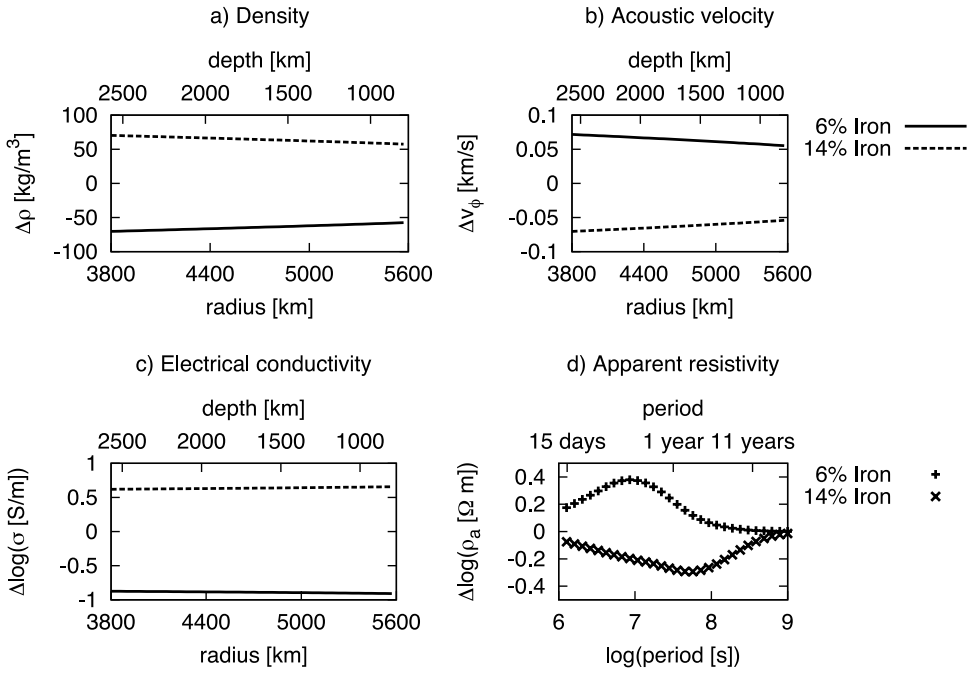

Figure 5. Effect of iron content on (a) the computation of lower mantle density, (b) acoustic wave speed, (c) electrical conductivity, and (d) apparent resistivity. Variations of geophysical data are computed for x_{Fe} = 6% and 14% and compared to the reference values at x_{Fe} = 10% (see Figure 2).

observation that the temperature effect is maximum at the middle of the period range and that resistivities converge toward identical values, whatever the model, at periods shorter and longer than 10^6 and 10^8 s, respectively, is explained by the boundary conditions that we impose at the top and at the bottom of the models. In particular, apparent reactivities at periods longer than 11 years are totally controlled by the high conductivity of the D″ layer and of the core (see section 2.1).

3.3.3. Iron Content

[48] The iron dependence of density ρ, acoustic speed v_ϕ, electrical conductivity σ and apparent resistivities ρ_a is shown in Figures 5a–5d. As can be seen from $\rho^{(i)}_{0,Fe}$ values in Table 2, density increases with iron content for both perovskite and magnesiowüstite. This leads to a 3% increase of the assemblage density for an increasing x_{Fe} from 6% to 14% (Figure 5a). To the best of our knowledge, current laboratory data do not provide evidence for a dependence of the value of the bulk modulus with respect to the iron content of lower mantle minerals (see section 3.2.1). Consequently, the effect of iron on the acoustic speed is directly related to the effect on density and an increase of x_{Fe} from 6 to 14% only produces a decrease in v_ϕ of about 1% (Figure 5b).

[49] As iron plays a major role in mineral conductivity mechanisms, the electrical conductivity increases considerably with the iron content: $\log(\sigma)$ increases by about 1.5 log unit if the iron content of the lower mantle is increased from 6% to 14%. The electrical conductivity is the most sensitive data to the iron content. The huge increase of the electrical conductivity induces a large effect on the apparent resistivities ρ_a. Figure 5d presents the variations of apparent resistivities for three different iron contents. The effect is the largest for periods around 10^7 s. At such periods, the apparent resistivities decrease by more than 0.5 log units for an increase of the iron content from 6% to 14%.

3.3.4. Summary: Complementarity of Electromagnetic and Seismic Data

[50] The effects of parameter variations on synthetic data, averaged over the depth range [800 km, 2600 km] are summarized in Table 4. The variations in the synthetic data are computed with respect to the adiabatic and pyrolitic reference model.

[51] Electromagnetic and seismic data are highly complementary for the determination of temperature and mineralogy of the lower mantle. They are ideally suited for deriving these properties from a joint inversion. The main physical reason for this complementarity is that rocks that exhibit an identical mechanical behavior (and can therefore not be distinguished on the basis of seismic data only) often have a distinct electrical behavior. The electrical conductivity increases with temperature and iron content, but decreases with perovskite content. Both acoustic speed v_ϕ and density ρ increase with perovskite content and decrease with temperature, but they present an opposite iron content dependence: v_ϕ decreases with iron content whereas ρ increases.

Table 4. Sensitivity of Geophysical Data to Temperature, Perovskite Content, and Iron Content, Averaged Over the Depth Range [800 km, 2600 km][a]

	ΔT = 400 K	ΔX_{pv} = 0.30	Δx_{Fe} = 0.4
$\Delta\rho/\rho$ (kg m^{-3})	-4.4×10^{-3}	8.2×10^{-3}	$\mathbf{1.3 \times 10^{-2}}$
$\Delta v_\phi/v_\phi$ (km s^{-1})	-4.6×10^{-3}	$\mathbf{4.6 \times 10^{-2}}$	-6.41×10^{-3}
$\Delta \log(\sigma)/\log(\sigma)$	**0.50**	−0.11	**1.17**

[a]The variations of the synthetic data are computed relative to the reference model, i.e., T adiabatic, X_{pv} = 80%, x_{Fe} = 10%. The highest sensitivities to parameter values are in boldface for each data.

[52] The acoustic wave speed is highly dependent on the perovskite content whereas the electrical conductivity is highly sensitive to the iron content and to a lesser extent, to the mean temperature of the lower mantle. Density depends slightly on the mineralogy and on the iron content of the lower mantle. The very different sensitivities of the data to the parameters indicate therefore that the covariance in an inversion of the selected geophysical data should be weak.

4. Inverse Problem

[53] In this section, we explain our stochastic inversion method and we validate it on synthetic geophysical data sets.

4.1. Bayesian Inversion Using Monte Carlo Markov Chain Method

[54] We only recall the fundamentals of the Bayesian inversion, based on the Monte Carlo Markov Chain method, that has been extensively detailed by previous workers, in particular, *Mosegaard and Tarantola* [1995], *Mosegaard* [1998], and *Khan et al.* [2006]. The inverse problem consists in computing the values of the parameters governing the internal structure of the Earth's lower mantle from the observed geophysical data. Let us denote by $\vec{p} = (p_1, p_2, \ldots, p_{30})$ the 30 parameters of our model and by $\vec{d} = (d_1, d_2, \ldots, d_{30})$ the 30 geophysical data that constrain them via the relation $\vec{d} = A(\vec{p})$, where the operator A represents the forward problem discussed in section 3. Explicitly, the parameters are the temperature profile $T(r)$, the volume fraction of perovskite $X_{\mathrm{pv}}(r)$, and the volume fraction of the bulk iron content $x_{\mathrm{Fe}}(r)$. The data are PREM acoustic wave speeds $v_\phi(r)$, PREM densities $\rho(r)$ and the discrete series of apparent resistivities computed from *Olsen* [1999] (see Table 1). Our model of the lower mantle is divided into ten layers of equal thickness. If we note by $\mathcal{M}_i$ the set of all values for the parameter i, the set $\mathcal{M}$ of all possible parameter configurations is equal to $\mathcal{M} = \otimes_{i=1}^{30}\mathcal{M}_i$. We choose to solve the inverse problem by a stochastic method, since the forward problem is strongly nonlinear.

[55] In the Bayesian framework, parameters and data are considered as random variables characterized by their probability density functions (pdf). The solution to the inverse problem consists in the computation of the a posteriori probability $P(p|d)$ that the parameters are in a configuration p given that the data are in a measured configuration d. Using Bayes' formula, this probability can be written as

$$P(p|d) = \frac{P(p \cap d)}{P(d)} = \frac{P(d|p)P(p)}{\sum_{p\in\mathcal{M}} P(d|p)P(p)} \tag{16}$$

The sum in the denominator runs over all the configurations p of $\mathcal{M}$. Two probabilities are present in Bayes' formula: the likelihood $P(d|p)$ and the prior probability $P(p)$.

[56] The likelihood $P(d|p)$ is a function of the misfit $S(d, A(p))$ which measures the difference between the observed data d and the computed synthetic data $A(p)$:

$$P(d|p) \propto e^{-S(d,A(p))} \tag{17}$$

The likelihood is related to the experimental noise which affects the measurement of the data d. This noise is assumed to be gaussian and we write

$$S = \sum_{l=1}^{10} \frac{\left(v_{\phi_l}^{obs} - v_{\phi l}^{calc}\right)^2}{2\,\gamma_{v_{\phi_l}}^2} + \sum_{l=1}^{10} \frac{\left(\rho_l^{obs} - \rho_l^{calc}\right)^2}{2\,\gamma_{\rho_l}^2} + \sum_{l=1}^{10} \frac{\left(\rho_{a_l}^{obs} - \rho_{a_l}^{calc}\right)^2}{2\,\gamma_{\rho_{al}}^2} \tag{18}$$

where the labels obs and calc refer to the sets of actually observed data d and of synthetic data $A(p)$, respectively. Uncertainties on the data d are described by the standard deviations γ.

[57] The prior probability $P(p)$ assigns to each configuration p a probability independently of the data. In our model, we assume that parameter values, i.e., perovskite fraction, temperature, and iron content, vary smoothly as a function of depth. According to *Besag and Kooperberg* [1995], we adopt a locally quadratic Gaussian prior which penalizes sharp local variations of the parameters, and we add a linear prior at both ends of the model:

$$P(p) \propto \lambda_p^{\frac{10}{2}} \exp\left\{ -\frac{1}{2}\lambda_p \left[(p_2 - p_1)^2 + \sum_{k=2}^{9} (p_{k-1} - 2p_k + p_{k+1})^2 + (p_{10} - p_9)^2 \right] \right\} \tag{19}$$

where λ_p is a prior coefficient whose value can be tuned to balance between minimizing the misfit and the roughness of the parameter profile.

[58] A quantity, very useful to look at the values that can be taken by a given parameter, is the marginal probability $P(p_i = x|d)$ obtained by summing all the probabilities of the configurations p whose ith parameter takes the value x. Explicitly,

$$P(p_i = x|d) = \frac{\sum_{p\in\mathcal{M}_x} P(d|p)\; P(p)}{\sum_{p\in\mathcal{M}} P(d|p)P(p)} \tag{20}$$

where $\mathcal{M}_x = \mathcal{M}_1 \otimes \ldots \otimes x \otimes \ldots \otimes \mathcal{M}_{30}$ denotes the whole set of configurations whose ith component is x. The expected value of the parameter p_i can be computed from the marginal probabilities $P(p_i = x|d)$ as

$$\sum_{x\in\mathcal{M}_i} xP(p_i = x|d) \tag{21}$$

[59] The denominators of the formulas (16) and (20) involve number of terms equal to $\Pi_{i=1}^{30}\,|\mathcal{M}_i|$, where $|\mathcal{M}_i|$ is the number of values that can be taken by the parameter i. Since these denominators are too large to be processed numerically, sophisticated techniques have been developed to estimate the marginal probabilities (20). These are the Monte Carlo Markov Chain methods (MCMC) [see, e.g., *Häggström*, 2002]. The basic idea of these methods is to build a random walk designed to sample the configuration space $\mathcal{M}$ according to the probability $P(p|d)$. Among the different MCMC algorithms, we choose the Metropolis

algorithm [*Metropolis et al.*, 1953]. The sampling of the configurations is characterized by an acceptance rate. The maximum efficiency of the algorithm is obtained for rate values close to 0.25 [*Gelman et al.*, 2003]. This value is used to tune the prior coefficients.

4.2. Joint Inversion of Synthetic Data

[60] Using the forward problem described in section 3, we compute density, acoustic speed and apparent resistivities for two initial sets of parameter values. Different kinds of temperature, iron fraction and perovskite content profiles are chosen in order to test the efficiency of the prior modeling, given the uncertainties on actual data. With the examples presented in the paper, our intention is to illustrate that the regularity condition that we use on the parameter profiles (equation (19)) and the penalization of sharp local variations allow us to recover temperature gradient variations and do not oversmooth strong local variations in parameter values. The first model, hereafter named model 1, corresponds to the temperature model proposed by *Matas et al.* [2007] for a derivative $\partial\mu/\partial P$ equal to 1.6 for perovskite. The geotherm is a second-order polynomial with a subadiabatic temperature gradient equal to 0.25 K km^{-1} at 800 km depth and temperature values equal to 1800 K and 2800 K at 800 and 2600 km depth, respectively. The second model (model 2) has a superadiabatic geotherm with potential temperature and linear temperature gradient equal to 1600 K and 0.5 K km^{-1}. Temperature values are equal to 2000 K and 2900 K at the top and at the bottom of the model, respectively. In both cases, the iron fraction increases linearly with depth, from 10 to 15%, and the model is divided into two subregions of perovskite content equal to 80% and 90% above and below 2060 km depth.

[61] The synthetic apparent resistivities are computed for a set of 10 periods reported by *Olsen* [1999] in the period range [10^6 s, 10^9 s] (Table 1). At each period, we use the uncertainty reported by *Olsen* [1999]. Using the MCMC inversion, we evaluate the a posteriori pdf on the parameter values corresponding to an uncertainty of 1% on the density and 0.5% on the acoustic wave speed.

[62] At each radius r, the variation range allowed for the inverted parameters are (1) $T \in$ [1500 K, 3500 K] (2) $X_{\mathrm{pv}} \in$ [0, 1], and (c) $x_{\mathrm{Fe}} \in$ [0.05, 0.25]. The latter parameter ranges are used to scale the values of the prior coefficients λ_p according to:

$$\lambda_p = \lambda/(p_{\max} - p_{\min})^2 \tag{22}$$

where $p_{\min}$ and $p_{\max}$ denote the bounds of each parameter range. The λ value is tuned in each inversion in order to obtain an acceptance rate close to the optimal value of 0.25.

[63] Figure 6 shows the comparison between the initial values of the parameters (gray curve) and their a posteriori estimates (mean values are represented by the black curve). Twenty millions iterations are performed. We sample the computed configurations every 2000 iterations, providing 10,000 samples models at each depth. Among these samples, the first 2000, corresponding to the burning stage of the stochastic process, are discarded and the a posteriori estimates are computed on 8000 sample models. Dashed curves with labels indicate the distribution of these sample models at each depth. Mean values are classically used to characterize probability distribution, but the significant output of a stochastic inversion is the whole probability distribution. It cannot be reduced to one estimator such as the mean or the median. Our interpretation is thus based on the whole distribution probability, not on the mean value alone. Down to 1700 km depth, whatever the parameters and the initial temperature profile, the maxima of the histograms fit the initial values very well. Because of the asymmetry of the histograms, the a posteriori mean temperature values are shifted toward higher values with respect to the initial temperature profile. This effect is particularly visible at shallow depths where it reaches at most 5%. In order to take this effect into account, the inversion results for PREM and *Olsen*'s [1999] data will be presented in terms of mean, median, and 1σ and 2σ bounds (see section 5). A loss of resolution is observed for depths greater than 1700 km. The misfit between initial and computed values becomes significant for temperatures higher than 2500 K, which corresponds to an electrical conductivity of about 25 S m^{-1}. We associate this resolution loss with the penetration depth of electromagnetic waves, which decreases with increasing conductivity. As a result, the longest period available (11 years) sounds the model down to 2100 km and 1700 km depth for model 1 and model 2, respectively. Beyond these depths, there is no constraint from electromagnetic data and the inversion process naturally converges toward the mean of the variation range allowed for temperature. A similar behavior is observed for the iron content, whereas the perovskite volume fraction is constrained by the whole set of geophysical data down to the bottom of the model. These results are coherent with the sensitivity analysis presented in section 3.3, which showed that electromagnetic data are mostly sensitive to temperature and iron content while seismic data mostly constrain the mineralogical composition. Note that the chosen prior permits to resolve the 10% jump in perovskite content that was imposed at 2060 km depth.

[64] We thus expect that the inversion of PREM and *Olsen*'s [1999] data will enable us to resolve the thermal state and the iron content of the lower mantle down to $\sim$2000 km depth, and the perovskite fraction over the whole depth range.

5. Inversion of PREM and Global Induction Data

5.1. Results

[65] The inversion results of PREM density and acoustic speeds and *Olsen*'s [1999] apparent resistivities are displayed in Figure 7 and listed in Table 5. The inversion scheme (prior, number of iterations, sampling method, and acceptance rate) is exactly the same as in section 4.2. Figure 7 (top) shows the a posteriori estimates of the temperature (Figure 7, left), iron content (Figure 7, middle) and perovskite fraction (Figure 7, right). As stated in section 4.2, our interpretation is based on the whole probability distribution, not on individual estimator values. In Figure 7 (bottom), actual data are compared with the synthetic data recomputed from the models.

[66] The resolved part of the temperature profile (i.e., in the depth range [800 km, 2000 km]) is divided into two subregions. From 800 km to 1300 km depth, the temperature is close to a value of 2200 K. Between 1300 km and 2000 km

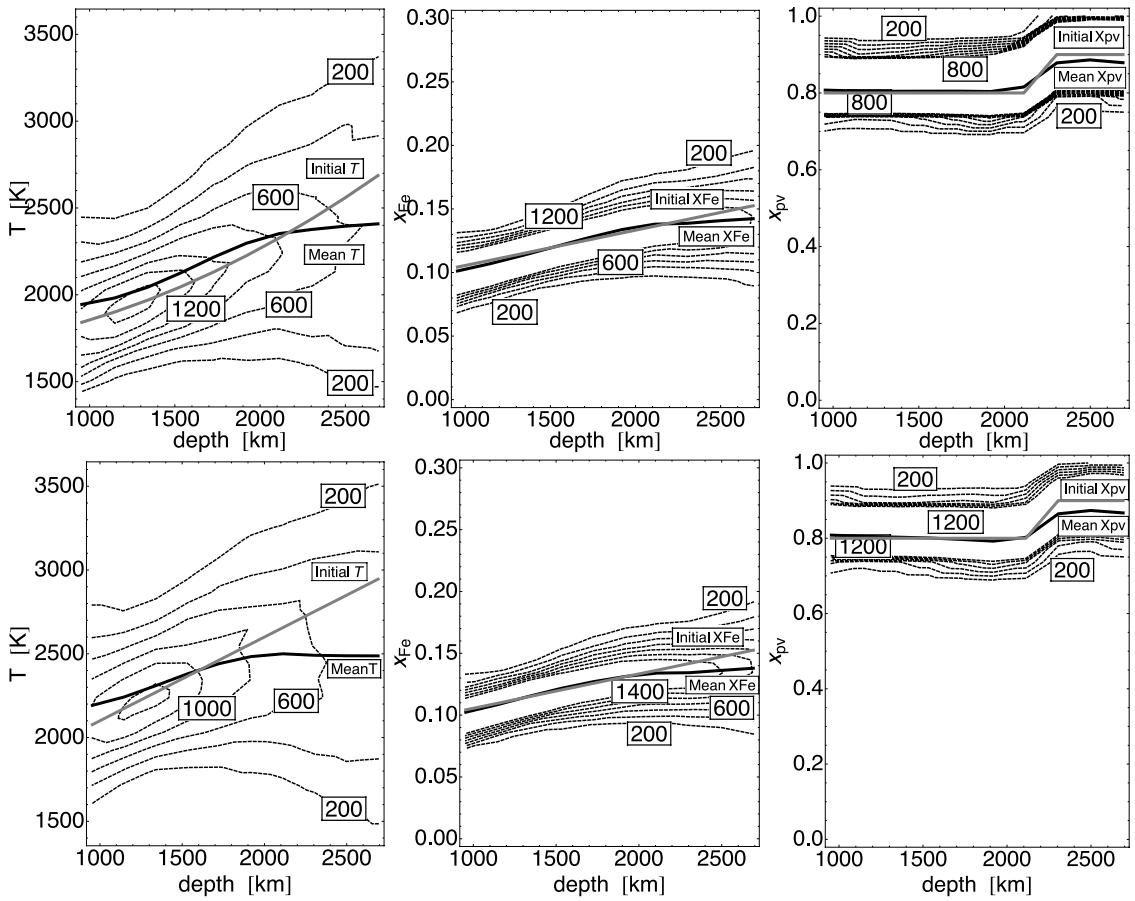

Figure 6. Results of synthetic tests for two parameter sets. (top) The geotherm is a second-order polynomial computed from *Matas et al.* [2007]. The temperature gradient is equal to 0.25 K km^{-1} at 800 km depth, and temperature values are equal to 1800 K and 2800 K at 800 and 2600 km depth, respectively. (bottom) Superadiabatic geotherm with potential temperature and linear temperature gradient equal to 1600 K and 0.5 K km^{-1}. Temperature values are equal to 2000 K and 2900 K at the top and at the bottom of the model, respectively. In both cases, the iron fraction increases linearly with depth, from 10 to 15%. The model is divided into two subregions of perovskite content equal to 80 and 90% above and below 2060 km depth. The gray curve corresponds to the initial value; the black curve represents mean values estimated by stochastic inversion of the synthetic data. Dashed curves with labels indicate the distribution of 8000 sample models at each depth. (left) Temperature; (middle) iron content; (right) perovskite fraction. Vertical axis span the range of values tested in the inversion.

depth, the temperature increases along a superadiabatic gradient of 0.4 K km^{-1}. Extrapolation of this gradient beyond 2000 km, i.e., in the unresolved region of the model, leads to a temperature close to 2800 K at 2600 km depth.

[67] Iron content values are restricted to the range [10%,11%] whatever the depth, while a significant linear decrease of the perovskite content is observed throughout the whole depth range, from 80% at 800 km depth down to ~65% at 2600 km depth. All parameter values are resolved with a 10–15% uncertainty at the 1σ confidence level.

[68] Our results refine and give a coherent insight on previously published interpretations based on seismic data alone. A superadiabatic thermal gradient associated with a change in mineralogical composition is consistent with the interpretation of *Cammarano et al.* [2005]. The decrease of the perovskite fraction with depth is in very good agreement with the results of *Deschamps and Trampert* [2004], although they obtained this result for a significantly (~300 K) colder geotherm and a lower value of the iron content (about 8%). The value x_{Fe} = 0.10 had also been obtained by *Mattern et al.* [2005] but for a subadiabatic geotherm. A superadiabatic temperature gradient of the order of 0.4 K km^{-1} is significantly lower than the value proposed by *Khan et al.* [2006] on the basis of *Olsen*'s [1999] electromagnetic data. Our results are in a general agreement with the model proposed *Matas et al.* [2007] for $(\partial\mu/\partial P)_{pv}$ = 1.6.

5.2. Discussion

[69] The temperature estimate that we obtained close to about 1000 km depth is in the range 2000–2500 K at 1σ confidence level. The interface between the transition zone and the lower mantle, at a depth close to 660 km, is mostly due to the ringwoodite decomposition into perovskite and magnesiowüstite [*Ringwood*, 1975], with some contribution from nonolivine component transformations [e.g., *Vacher et al.*, 1998]. The ringwoodite decomposition occurs at a

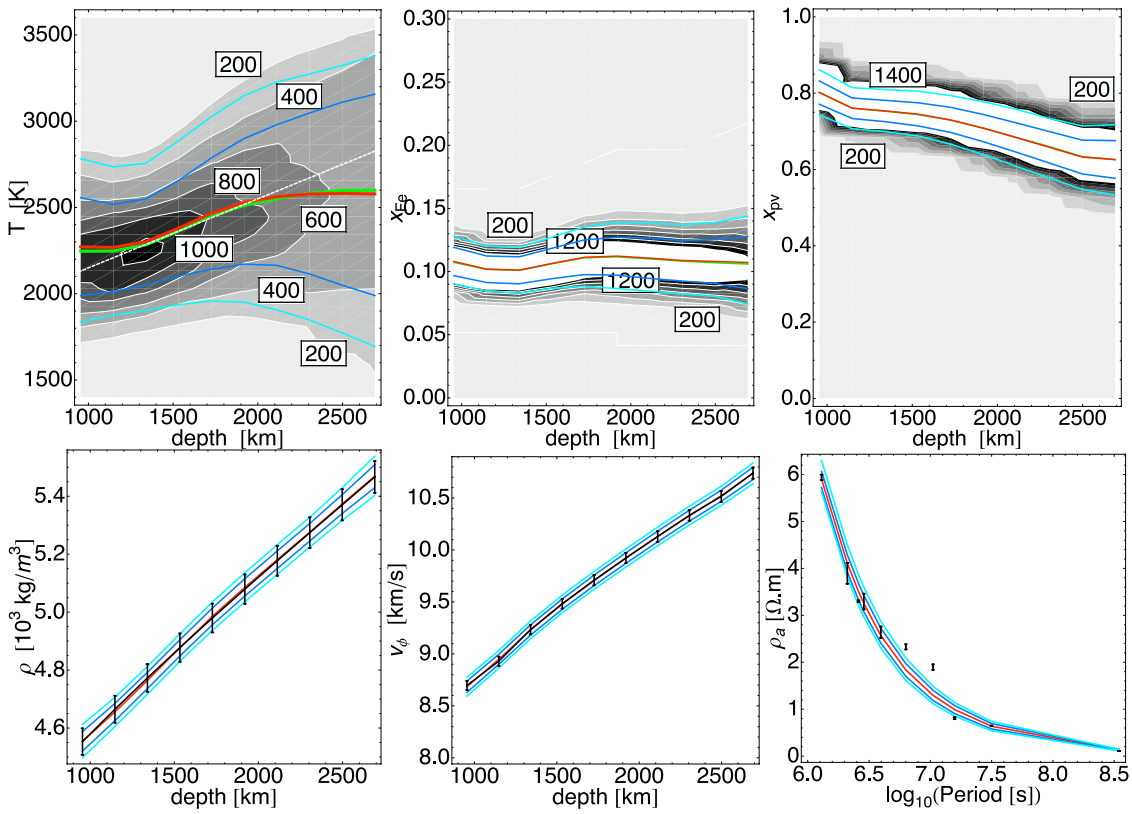

Figure 7. Stochastic inversion of PREM and *Olsen*'s [1999] data. (top) Empirical histograms for (left) temperature, (middle) iron content, and (right) perovskite fraction in the lower mantle. The red and green curves are the mean and median values, respectively. For iron content and perovskite fraction, both curves are superimposed. Shaded contours with labels indicate the distribution of 8000 sample models at each depth. Vertical axis span the range of values tested in the inversion. For temperature, the dashed curve is drawn for an adiabatic geotherm with a linear temperature gradient equal to 0.4 K km^{-1}. In the latter case, temperature values are equal to 2070 K and ~2800 K at 800 and 2600 km depth, respectively. (bottom) Comparison between actual (dots with 1σ error bars) and synthetic data recomputed from the models. Dark and light blue curves are drawn at the 1σ and 2σ confidence levels, respectively.

temperature close to 1873 ± 150 K [*Ito and Takahashi*, 1989]. This uncertainty of about 10% associated to both measurements, impedes any conclusion about the value of the temperature gradient at the top of the lower mantle.

[70] We now discuss some assumptions and choices present in this work. The first one corresponds to the choice of data to be inverted. In this work, we considered that apparent resistivities are the electromagnetic counterpart of seismic speeds. Both are processed data from a set of geophysical observations recorded at the Earth surface and are suitable to describe a one-dimensional structure of the lower mantle. Another option would have been to choose seismic travel times and modal frequencies of the Earth's free oscillations instead of density and seismic speeds. The

Table 5. Parameter Statistics From a Joint Inversion of *Olsen*'s [1999] Apparent Resistivities, PREM Densities, and PREM Acoustic Speeds[a]

depth (km)	T Median (K)	T Mode (K)	1σ bounds (K)		x_{Fe} Median	1σ bounds		X_{pv} Median	1σ bounds	
954	2247 (2132)	2100	1988	2557	0.11	0.10	0.12	0.80	0.77	0.84
1147	2248 (2209)	2200	2013	2518	0.10	0.09	0.11	0.76	0.73	0.79
1340	2283 (2286)	2200	2050	2550	0.10	0.09	0.11	0.75	0.72	0.79
1533	2363 (2363)	2300	2102	2658	0.11	0.09	0.12	0.74	0.71	0.78
1726	2449 (2440)	2400	2142	2788	0.11	0.10	0.13	0.73	0.69	0.77
1919	2512 (2518)	2400	2171	2900	0.11	0.10	0.13	0.71	0.67	0.75
2112	2551 (2595)	2400	2164	2980	0.11	0.09	0.13	0.68	0.64	0.73
2305	2583 (2672)	2500	2115	3048	0.11	0.09	0.12	0.66	0.61	0.71
2498	2598 (2749)	2500	2050	3110	0.11	0.09	0.13	0.63	0.58	0.68
2691	2600 (2826)	2900	1989	3157	0.11	0.09	0.13	0.63	0.57	0.68

[a]Depth values correspond to the bottom of the layers. Top of first layer is located at 800 km depth. Median values and 1σ bounds are reported for temperature T, iron content x_{Fe}, and perovskite fraction X_{pv}. Values in italics are not constrained by the data. Temperature values in parentheses correspond to a superadiabatic gradient of 0.4 K km^{-1} extrapolated from the [1340 km, 1919 km] domain (dashed curve in Figure 7). Modal values for temperature correspond to the histograms of Figure 7. They are computed with temperature steps of 100 K.

electromagnetic counterpart of these seismic data are the variations of the Earth's magnetic field. Bayesian inversion of magnetic field variations along with seismic travel times and modal frequencies of the Earth's free oscillations is however impossible to realize at present time, due to the huge computer time needed to compute the associated forward problem. Note also that a rigorous inversion of travel times would also need a relocation of the seismic events.

[71] Concerning the parameterization of the model, we did not consider the possible presence of volatile elements like water, nor some possible spin transitions inside lower mantle mineral phases. The presence of water in the upper mantle and transition zone may have important effects on the data but, to the best of our knowledge, there is no definitive evidence for a significant presence of water in the lower mantle. This is the reason why we restrict the domain of inversion to the 800–2600 km depth range, without any attempt to explain the values of upper mantle electrical conductivity in terms of structure, thermal state or composition. Our choice of working with apparent resistivities at periods longer than 15 days guarantees that our results are not affected by the electric modeling of the upper mantle.

[72] A spin transition in iron of magnesiowüstite has been recently observed at the pressure relevant to the Earth's lower mantle. This transition induces an abnormal compressional behavior of the mineral [*Lin et al.*, 2005] and a possible variation of its electrical conductivity at high temperature. *Lin et al.* [2007] observed this conductivity variation at temperature around 500 K, but they pointed out that the effect of the spin transition at temperatures higher than 1000 K is presently unknown. This is the reason why this transition is not yet included in the inversion.

[73] In view of the poorly known behavior of the shear modulus at high temperature and high pressure, we inverted acoustic speed only. An additional increase of the resolution power of our method would likely be obtained once shear properties would be refined by laboratory experiments.

[74] An improvement of our inversion technique will be to take into account the uncertainties of laboratory measurements (Tables 2 and 3) in the inversion scheme. Such an improvement is challenging regarding both the required computer time and the difficulty to associate to each elastic and electrical property the probability distributions, inherent to each measurement.

6. Conclusion

[75] In order to overcome the composition temperature trade-off encountered in the inversion of the sole seismic data, we constrained independently the temperature, the iron content and the mineralogy of the lower mantle by a joint inversion of electromagnetic and seismic data.

[76] By computing density, acoustic speed and apparent resistivity for different sets of temperature and composition profiles, we have quantified the complementarity of the different geophysical observables. Apparent resistivities are mostly sensitive to temperature and iron content, while densities and acoustic speeds mostly constrain the mineralogy. A 400 K increase of temperature increases the electrical conductivity by about 0.5 log units and $\log(\sigma)$ increases by about 1.5 log unit if the iron content of the lower mantle is increased from 6% to 14%. Acoustic velocity increases by 0.8 km s^{-1} on average as the perovskite fraction increases from 50% to 100%.

[77] The resolving power of a Bayesian inversion method based on the Metropolis algorithm has been validated on synthetic data. The results of the synthetic test demonstrate the ability of the data and the inversion method to detect first-order variation of the temperature gradient together with strong chemical (iron content) variation, if any. Given the uncertainties on actually observed data, estimates of perovskite fraction are well recovered over the whole depth range, while information on temperature and iron content is limited to a depth of about 2000 km, as a consequence of the limited penetration depth of the longest period of electromagnetic waves induced by external sources.

[78] We have jointly inverted *Olsen*'s [1999] apparent resistivities in the period range [15 days, 11 years], and PREM densities and acoustic speeds, to derive estimates of the composition and temperature of the lower mantle in the depth range [800 km, 2600 km]. The iron content of the lower mantle is found to be almost constant and equal to 10–11% whatever the depth, while a significant linear decrease of the perovskite fraction is observed throughout the whole depth range, from 80% at 800 km depth down to ~65% at 2600 km depth. The temperature in the uppermost lower mantle (i.e., down to 1300 km depth) is found to be close to a value of 2200 K. Between 1300 and 2000 km depth, the temperature increases along a superadiabatic gradient of 0.4 K km^{-1}. The extrapolation of this gradient at greater depth leads to a temperature value close to 2800 K at 2600 km depth (Figure 7). Since temperature values at the core-mantle boundary are expected to be in the range 3800 ± 500 K [*Lay et al.*, 2008], our model would also imply the presence of a thermal boundary layer at the bottom of the lower mantle.

[79] **Acknowledgments.** This work was initiated during O.V.'s postdoctoral fellowship at Nantes University supported by the European Community's Improving Human Potential Programme. A.R. is acknowledging the support of the Belgian Science Policy Office (PRODEX). The research of O.V. was supported by Belgian Federal Science Policy Office Action 1 and FNRS (Scientific Research Worker position). Part of this work was performed when A.M. was visiting Professor in Bruxelles and O.V. in Nantes. We acknowledge the support of a Tournesol grant from the Belgian CGRI and Egide Programme. We also thank the FNRS in Belgium and the CNRS PNP in France for support. The authors are grateful to N. Olsen for providing them with sets of impedances. This paper benefited from the constructive comments of the Associate Editor, M. H. Ritzwoller, and two anonymous reviewers.

References

Alldredge, L. R. (1977), Deep mantle conductivity, *J. Geophys. Res.*, *82*, 5427–5431.

Anderson, D. L. (1988), Temperature and pressure derivatives of elastic constants with application to the mantle, *J. Geophys. Res.*, *93*, 4688–4700.

Banks, R. J. (1969), Geomagnetic variations and the electric conductivity of the upper mantle, *Geophys. J. R. Astron. Soc.*, *17*, 457–487.

Besag, J., and C. Kooperberg (1995), On conditional and intrinsic autoregression, *Biometrika*, *82*, 733–746.

Birch, F. (1952), Elasticity and the constitution of the Earth's interior, *J. Geophys. Res.*, *57*, 227–286.

Buffett, B. A., P. M. Mathews, and T. A. Herring (2002), Modeling of nutation and precession: Effects of electromagnetic coupling, *J. Geophys. Res.*, *107*(B4), 2070, doi:10.1029/2000JB000056.

Cammarano, F., S. Goes, P. Vacher, and D. Giardini (2003), Inferring upper mantle temperatures from seismic velocities, *Phys. Earth Planet. Inter.*, *138*, 197–222.

Cammarano, F., S. Goes, A. Deuss, and D. Giardini (2005), Is a pyrolytic adiabatic mantle compatible with seismic data?, *Earth Planet Sci. Lett.*, *232*, 227–243.

Currie, R. G. (1968), Geomagnetic spectrum of internal origin and lower mantle conductivity, *J. Geophys. Res.*, *73*, 2779–2786.

Deschamps, F., and J. Trampert (2004), Towards a lower mantle reference temperature and composition, *Earth Planet. Sci. Lett.*, *222*, 161–175.

Dobson, D. P., and J. P. Brodholt (2000), The electrical conductivity of the lower mantle phase magnesiowüstite at high temperatures and pressures, *J. Geophys. Res.*, *105*, 531–538.

Dziewonski, A. M., and D. L. Anderson (1981), Preliminary reference Earth model, *Phys. Earth Planet. Inter.*, *25*, 297–356.

Fiquet, G., D. Andrault, A. Dewaele, T. Charpin, M. Kunz, and D. Haüserman (1998), P-V-T equation of state of $MgSiO_3$ perovksite, *Phys. Earth Planet. Inter.*, *105*, 21–31.

Fiquet, G., A. Dewaele, D. Andrault, M. Kunz, and T. L. Bihan (2000), Thermoelastic properties and crystal structure of $MgSiO_3$ perovskite at lower mantle pressure and temperature conditions, *Geophys. Res. Lett.*, *27*, 21–24.

Gelman, A., J. B. Carlin, H. S. Stern, and D. B. Rubin (2003), *Bayesian Data Analysis*, Chapman and Hall, Boca Raton, Fla.

Gong, Z., Y. Fei, F. Dai, L. Zhang, and F. Jing (2004), Equation of state and phase stability of mantle perovskite up to 140 GPa shock pressure and its geophysical implications, *Geophys. Res. Lett.*, *31*, L04614, doi:10.1029/2003GL019132.

Green, D. H., and T. J. Falloon (1998), Pyrolite: A ringwood concept and its current expression, in *The Earth's Mantle: Structure, Composition and Evolution*, edited by I. Jackson, pp. 311–378, Cambridge Univ. Press, Cambridge, U. K.

Häggström, O. (2002), *Finite Markov Chains and Algorithmic Applications*, 124 pp., Cambridge Univ. Press, Cambridge, U. K.

Hashin, Z., and S. Shtrikman (1962), A variational approach to the theory of the effective magnetic permeability of multiphase materials, *J. Appl. Phys.*, *33*, 3125–3131.

Hashin, Z., and S. Shtrikman (1963), A variational approach to the theory of the elastic behaviour of multiphase materials, *J. Mech. Phys. Solids*, *11*, 127–140.

Holme, R. (1998), Electromagnetic core-mantle coupling - I. Explaining decadal changes in the length of day, *Geophys. J. Int.*, *132*, 167–180, doi:10.1046/j.1365-246x.1998.00424.x.

Ito, E., and E. Takahashi (1989), Postspinel transformations the system Mg_2SiO_4–Fe_2SiO_4 and some geophysical implications, *J. Geophys. Res.*, *94*, 10,637–10,646.

Jackson, I. (1998), Elasticity, composition and temperature of the Earth's lower mantle: A reappraisal, *Geophys. J. Int.*, *134*, 291–311.

Jacobsen, S. D., H.-J. Reichmann, H. A. Spetzler, S. J. Mackwell, J. R. Smyth, R. J. Angel, and C. A. McCammon (2002), Structure and elasticity of single-crystal (Mg,Fe)O and a new method of generating shear waves for gigahertz ultrasonic interferometry, *J. Geophys. Res.*, *107*(B2), 2037, doi:10.1029/2001JB000490.

Kennett, B. L. N., E. R. Engdahl, and R. Buland (1995), Constraints on seismic velocities in the Earth from traveltimes, *Geophys. J. Int.*, *122*, 108–124.

Khan, A., J. A. D. Connolly, and N. Olsen (2006), Constraining the composition and thermal state of the mantle beneath Europe from inversion of long-period electromagnetic sounding data, *J. Geophys. Res.*, *111*, B10102, doi:10.1029/2006JB004270.

Kiefer, B., L. Stixrude, and R. M. Wentzcovitch (2002), Elasticity of $(Mg,Fe)SiO_3$-perovskite at high pressures, *Geophys. Res. Lett.*, *29*(11), 1539, doi:10.1029/2002GL014683.

Lay, T., J. Hernlund, and B. A. Buffett (2008), Core-mantle boundary heat flow, *Nat. Geosci.*, *1*, 25–32.

Li, B., and J. Zhang (2005), Pressure and temperature dependence of elastic wave velocity of MgSiO3 perovskite and the composition of the lower mantle, *Phys. Earth Planet. Inter.*, *151*, 143–154.

Lin, J.-F., V. V. Struzhkin, S. D. Jacobsen, M. Y. Hu, P. Chow, J. Kung, H. Liu, H.-K. Mao, and R. J. Hemley (2005), Spin transition of iron in magnesiowüstite in Earth's lower mantle, *Nature*, *436*, 377–380.

Lin, J.-F., S. T. Weir, D. D. Jackson, W. J. Evans, Y. K. Vohra, W. Qiu, and C.-S. Yoo (2007), Electrical conductivity of the lower-mantle ferropericlase across the electronic spin transition, *Geophys. Res. Lett.*, *34*, L16305, doi:10.1029/2007GL030523.

Mandea, M., D. Gibert, J.-L. Le Mouël, G. Hulot, and G. Saracco (1999), An estimate of average lower mantle conductivity by wavelet analysis of geomagnetic jerks, *J. Geophys. Res.*, *104*, 17,735–17,745.

Matas, J., and M. S. T. Bukowinski (2007), On the anelastic contribution to the temperature dependence of lower mantle seismic velocities, *Earth Planet. Sci. Lett.*, *259*, 51–61.

Matas, J., J. Bass, Y. Ricard, E. Mattern, and M. S. T. Bukowinski (2007), On the bulk composition of the lower mantle: Predictions and limitations from generalized inversion of radial seismic profiles, *Geophys. J. Int.*, *170*, 764–780.

Mattern, E., J. Matas, Y. Ricard, and J. Bass (2005), Lower mantle composition and temperature from mineral physics and thermodynamic modelling, *Geophys. J. Int.*, *160*, 973–990.

Menvielle, M., J. C. Rossignol, and P. Tarits (1982), The coast effect in terms of deviated electric currents: A numerical study, *Phys. Earth Planet. Inter.*, *28*, 118–128.

Metropolis, N., A. Rosenbluth, M. Rosenbluth, A. Teller, and E. Teller (1953), Equations of state calculations by fast computing machines, *J. Chem. Phys.*, *21*, 1087–1092.

Mosegaard, K. (1998), Resolution analysis of general inverse problems through inverse Monte-Carlo sampling, *Inverse Problems*, *14*, 405–426.

Mosegaard, K., and A. Tarantola (1995), Monte-Carlo sampling of solutions to inverse problems, *J. Geophys. Res.*, *100*, 12,431–12,447.

Murakami, M., K. Hirose, K. Kawamura, N. Sata, and Y. Ohishi (2004), Post-perovskite phase transition in $MgSiO_3$, *Science*, *374*, doi:10.1126/science.1095932.

Olsen, N. (1999), Long-period (30 days-1 year), Electromagnetic sounding and the electrical conductivity of the lower mantle beneath Europe, *Geophys. J. Int.*, *138*, 179–187.

Poirier, J.-P. (2000), *Introduction to the Physics of the Earth's Interior*, 312 pp., Cambridge Univ. Press, Cambridge, U.K.

Poirier, J.-P., and J. Peyronneau (1992), Experimental determination of the electrical conductivity of the material of the Earth's lower mantle, in *High-Pressure Research: Application to Earth and Planetary Sciences*, edited by Y. Syono and M. H. Manghnani, pp. 77–87, TERRAPUB, Tokyo.

Ringwood, A. E. (1975), *Composition and Petrology of the Earth's Mantle*, McGraw-Hill, New-York.

Saxena, S. K., and G. Shen (1992), Assessed data on heat capacity, thermal expansion, and compressibility for some oxides and silicates, *J. Geophys. Res.*, *97*, 19,813–19,825.

Semenov, V. Y., and W. Jozwiak (2006), Lateral variations of the mid-mantle conductance beneath Europe, *Tectonophysics*, *416*, 279–288.

Shankland, T. J., J. Peyronneau, and J.-P. Poirier (1993), Electrical conductivity of the Earth's lower mantle, *Nature*, *366*, 453–455.

Sinogeikin, S. V., J. Zhang, and J. D. Bass (2004), Elasticity of single crystal and polycristalline $MgSiO_3$ perovskite by Brillouin spectroscopy, *Geophys. Res. Lett.*, *31*, L06620, doi:10.1029/2004GL019559.

Srivastava, S. P. (1966), Theory of the magnetotelluric method for a spherical conductor, *Geophys. J. R. Astron. Soc.*, *11*, 373–387.

Stacey, F. D., and D. E. Loper (2007), A revised estimate of the conductivity of iron alloy at high pressure and implications for the core energy balance, *Phys. Earth Planet. Inter.*, *161*, 13–18.

Stixrude, L., and C. Lithgow-Bertelloni (2005), Thermodynamics of mantle minerals-I. Physical properties, *Geophys. J. Int.*, *162*, 610–632.

Tarits, P. (1994), Electromagnetic studies of global geodynamic processes, *Surv. Geophys.*, *15*, 209–238.

Trampert, J., P. Vacher, and N. Vlaar (2001), Sensitivities of seismic velocities to temperature, pressure and composition in the lower mantle, *Phys. Earth Planet. Inter.*, *124*, 255–267.

Vacher, P., and O. Verhoeven (2007), Modelling the electrical conductivity of iron-rich minerals for planetary applications, *Planet. Space Sci.*, *55*, doi:10.1016/j.pss.2006.10.003.

Vacher, P., A. Mocquet, and C. Sotin (1998), Computation of seismic profiles from mineral physics: the importance of the non-olivine components for explaining the 660 km depth discontinuity, *Phys. Earth Planet. Inter.*, *106*, 275–298.

Van Westrenen, W., et al. (2005), Thermoelastic properties of $(Mg_{0.64}Fe_{0.36})O$ ferropericlase based on in situ X-ray diffraction to 26.7 GPa and 2173 K, *Phys. Earth Planet. Inter.*, *151*, 163–176.

Verhoeven, O., et al. (2005), Interior structure of terrestrial planets: Modeling Mars' mantle and its electromagnetic, geodetic, and seismic properties, *J. Geophys. Res.*, *110*, E04009, doi:10.1029/2004JE002271.

Xu, Y., T. J. Shankland, and B. T. Poe (2000), Laboratory-based electrical conductivity in the Earth's mantle, *J. Geophys. Res.*, *105*, 27,865–27,875.

P.-A. Arrial, G. Choblet, A. Mocquet, P. Vacher, and O. Verhoeven, Laboratoire de Planétologie et Géodynamique, UMR 6112, UFR des Sciences et des Techniques, Université de Nantes, Nantes Atlantique Universités, CNRS, 2, rue de la Houssinière, BP 92 208, F-44322 Nantes CEDEX 3, France. (Pierre-Andre.Arrial@univ-nantes.fr; Gael.Choblet@univ-nantes.fr; Antoine.Mocquet@univ-nantes.fr; Pierre.Vacher@univ-nantes.fr; Olivier.Verhoeven@univ-nantes.fr)

V. Dehant, A. Rivoldini, and T. Van Hoolst, Royal Observatory of Belgium, 3 Avenue Circulaire, B-1180 Bruxelles, Belgium. (veronique.dehant@oma.be; rivoldini@oma.be; timvh@oma.be)

M. Menvielle, LATMOS, IPSL, UMR, UBSQ 8639, Observatoire de Saint-Maur and Université Paris-Sud, CNRS, F-94100 Saint Maur des Fossés, France. (michel.menvielle@cetp.ipsl.fr)

P. Tarits, UEB, UBO, IUEM, Place Nicolas Copernic, F-29280 Plouzané, France. (tarits@univ-brest.fr)